Personalized model adaptation for bioimpedance measurements optimization

A. A. DANILOV[*†], V. K. KRAMARENKO[†], D. V. NIKOLAEV[‡], and A. S. YUROVA[§]

Abstract — In this work we propose several techniques for personalized model adaptation, including anthropometrical scaling, control point mapping and geometrical modification of the body extremities positions. We compare our previous results of segmental bioimpedance analysis using the Visible Human Project (VHP) man model to the modified model with a corrected position of the arms.

Bioelectrical impedance analysis (BIA) is commonly used for body composition and abdominal adiposity assessment. BIA is also used in monitoring body fluid redistribution under various physiological and pathological conditions. The basics of the bioelectrical impedance theory are well covered in [10, 13]. The conventional measurement technique involves two pairs of electrodes attached to the skin. One pair, labeled *current carrying* (CC) electrodes, is used for injecting electrical current into the body. The second pair, labeled *pick-up* (PU) electrodes, is used for measuring the electric potential difference. This difference divided by the value of the injected current is called the *transfer impedance*.

The computational analysis of the existing measurement schemes is essential for accurate data interpretation and the development of new electrode schemes. One of the approaches is based on the calculation of the relative contribution of the tissues and organs to the result of bioimpedance measurements of the particular body segment. In our previous work [3–5] we aimed at numerical modelling of BIA using the finite element method (FEM), construction and visualization of sensitivity field distributions using anatomically accurate 3D models of the human body from the Visible Human Project (VHP) [16]. A similar approach had been used earlier with partially segmented models of the human body [2, 11, 17].

[*]Institute of Numerical Mathematics, Russian Academy of Sciences, Moscow 119333, Russia. E-mail: a.a.danilov@gmail.com

[†]Moscow Institute of Physics and Technology, Dolgoprudny 141700, Russia

[‡]Scientific Research Center 'Medass', Moscow 101000, Russia

[§]Moscow State University, Department of Computational Mathematics and Cybernetics, Moscow 119991, Russia

The preparation of a 3D model takes a lot of time. It consists of two stages: image segmentation and mesh generation. While the latter may be automated using tetrahedral mesh generation techniques, the former still requires a lot of manual operations. We are focusing on the fullsize patient-specific high resolution 3D models. An accurate 3D model requires high resolution patient data like CT or MRI for the whole body, which in most cases is not available. However the anthropometrical measurements of the body are easily accessible, and in some cases we may have local CT/MRI images with patient-specific features. In this work we propose several techniques for adaptation of the once segmented human model to different patients or different measurement conditions, including anthropometrical scaling, control points mapping and geometrical modification of the body extremities positions. The last one may be crucial in modelling measurement techniques involving the specific position of the patient, as it may influence the results of the measurements.

The outline of the paper is as follows. In Section 2 we state the mathematical model and the theory of sensitivity analysis. In Section 3 we propose the mapping adaptation techniques. In Section 4 we describe the extremities position adaptation process and present the numerical results for segmented bioimpedance measurements.

1. Mathematical model and sensitivity analysis

In our previous work [4] we have proposed the mathematical model of bioimpedance measurements. The underlying equations are:

$$\text{div}(\mathbf{C}\nabla U) = 0 \quad \text{in } \Omega \tag{1.1}$$

$$(\mathbf{J}, \mathbf{n}) = I_0/S_\pm \quad \text{on } \Gamma_\pm \tag{1.2}$$

$$(\mathbf{J}, \mathbf{n}) = 0 \quad \text{on } \partial\Omega\backslash\Gamma_\pm \tag{1.3}$$

$$U(x_0, y_0, z_0) = 0 \tag{1.4}$$

$$\mathbf{J} = \mathbf{C}\nabla U. \tag{1.5}$$

In these equations Ω is the computational domain, $\partial\Omega$ is its boundary, $\Gamma_\pm$ are the electrode contact surfaces, $\mathbf{n}$ is the external unit normal vector, U is the electric potential, $\mathbf{C}$ is the conductivity tensor, $\mathbf{J}$ is the current density, I_0 is the electric current, $S_\pm$ are the areas of the electrode contacts. Equation (1.1) determines the distribution of the electric field over the domain with heterogeneous conductivity $\mathbf{C}$. Equation (1.2) sets the constant current density on the electrode contact surfaces. Equation (1.3) defines the no-flow condition on the boundary. The uniqueness of the solution is guaranteed by equation (1.4), where (x_0, y_0, z_0) is some point inside the domain Ω.

The values U, $\mathbf{C}$, I_0, and $\mathbf{J}$ in this study are considered to be real-valued, which corresponds to the active part of resistivity.

In our study we use the finite element method for solving (1.1)–(1.5) with P_1 finite elements on unstructured tetrahedral meshes. We assume that each computational element has a constant conductivity coefficient, which corresponds to one of the human tissues. The process of mesh generation is described in [4, 15] under the assumption that a segmented multimaterial model is given. In our work we opt for the Delaunay triangulation algorithm from the CGAL-Mesh library [14]. This algorithm enables defining a specific mesh size for each model material. In order to preserve the geometrical features of the segmented model, while keeping a feasible number of vertices, we assign a smaller mesh size to the blood vessels and a larger mesh size to the fat and muscle tissues. After initial mesh generation we apply mesh cosmetics from the Ani3D package [1]. This essential step reduces the FEM discretization errors and the condition number of the resulting stiffness matrices. After the mesh generation, we add a thin skin layer and the multilayered electrodes to the surface of the constructed mesh. The boundary triangulation is used to create a prismatic mesh on the surface. Each prism element is replaced by three tetrahedra.

As described in [9, 10], we introduce the reciprocal lead field $\mathbf{J}'_{\text{reci}}$ which is equal to the density vector field generated by a unit current excitation using the two PU electrodes. Field $\mathbf{J}'_{\text{reci}}$ is computed from (1.1)–(1.5), with the electrode surfaces $\Gamma_\pm$ corresponding to PU electrodes and $I_0 = 1$.

The lead field may be used for sensitivity distribution analysis of the PU electrodes for CC electrodes. We will use the following two equations: the general transfer signal equation

$$u = \int_\Omega \rho\, \mathbf{J}_{\text{cc}} \cdot \mathbf{J}'_{\text{reci}} \, \mathrm{d}x \qquad (1.6)$$

and the general transfer impedance equation:

$$Z_{\text{t}} = \int_\Omega \rho\, \mathbf{J}'_{\text{cc}} \cdot \mathbf{J}'_{\text{reci}} \, \mathrm{d}x. \qquad (1.7)$$

In these equations u is the measured signal between the PU electrodes, ρ is the resistivity, $\mathbf{J}_{\text{cc}}$ is computed from (1.1)–(1.5) with the electrode surfaces $\Gamma_\pm$ corresponding to the current-carrying electrodes, Z_{t} is the transfer impedance, and $\mathbf{J}'_{\text{cc}} = \mathbf{J}_{\text{cc}}/I_0$.

The sensitivity analysis is based on the distribution of the sensitivity field, which is computed by

$$S = \mathbf{J}'_{\text{cc}} \cdot \mathbf{J}'_{\text{reci}}. \qquad (1.8)$$

Using this notation we have the following relations:

$$Z_{\text{t}} = \int_\Omega \rho\, S \, \mathrm{d}x, \quad \Delta Z_{\text{t}} = \int_\Omega \Delta\rho\, S \, \mathrm{d}x. \qquad (1.9)$$

The last relation is applicable only for relatively small changes in ρ and moderate variations of S.

For sensitivity analysis purposes we will split Ω in three parts according to the value of the sensitivity field:

$$\Omega^- = \{\mathbf{x} | S(\mathbf{x}) < 0\}, \quad \Omega^+ = \{\mathbf{x} | S(\mathbf{x}) > 0\}, \quad \Omega^0 = \{\mathbf{x} | S(\mathbf{x}) = 0\}. \qquad (1.10)$$

Furthermore, for a specific threshold value $t \in [0, 100]$ we will define W_t^- as a subdomain of Ω^- and W_t^+ as a subdomain of Ω^+ with the following restrictions:

$$\inf_{\mathbf{x} \in \Omega \backslash W_t^-} \rho(\mathbf{x})S(\mathbf{x}) \geqslant \sup_{\mathbf{x} \in W_t^-} \rho(\mathbf{x})S(\mathbf{x}), \quad \int_{W_t^-} \rho\,S\,dx = \frac{t}{100} \int_{\Omega^-} \rho\,S\,dx \qquad (1.11)$$

$$\sup_{\mathbf{x} \in \Omega \backslash W_t^+} \rho(\mathbf{x})S(\mathbf{x}) \leqslant \inf_{\mathbf{x} \in W_t^+} \rho(\mathbf{x})S(\mathbf{x}), \quad \int_{W_t^+} \rho\,S\,dx = \frac{t}{100} \int_{\Omega^+} \rho\,S\,dx. \qquad (1.12)$$

In other words, W_t^+ is the region of high positive sensitivity values, which have the transfer impedance contribution equal to t percent of the total transfer impedance. The same applies to W_t^-, which is the region of the most negative sensitivity values.

We will also define in the same way the subdomains V_t^+ and V_t^+:

$$\sup_{\mathbf{x} \in \Omega \backslash V_t^\pm} \pm S(\mathbf{x}) \leqslant \inf_{\mathbf{x} \in V_t^\pm} \pm S(\mathbf{x}), \quad \int_{V_t^\pm} S\,dx = \frac{t}{100} \int_{\Omega^\pm} S\,dx. \qquad (1.13)$$

These regions are the most sensitive regions of small local resistivity changes.

In our sensitivity analysis we investigate the shape of the subdomains W_t^+ and V_t^+. These body regions represent the most sensitive parts of the human body in the specific measuring scenario. The shape of W_t^+ describes the part of the body in which one measures the transfer impedance. The shape of V_t^+ represents the part which is the most sensitive to local changes of conductivity. This analysis may be applied for the validation of empirically designed electrode schemes.

2. Adaptation to the body constitution

In our previous work we created fullsize segmented models of male and female human bodies [3, 5]. The segmentation process is a tedious work, and requires a lot of processing time. The existing technologies of semi-automatic segmentation can speed-up the work, however, creating a new personalized segmented model from scratch is a very time-consuming process so far. Assuming we already have a segmented model of some individual, we propose the methods for patient-oriented adaptation.

The most simple approach is the anthropometrical rescaling of the model. We split the reference model in several parts, and adjust their heights, according to the heights of the related parts of the patient. After that we also adjust the width of these parts according to the patient measurements. The schematic view of the proposed adaptation is presented in Fig. 1.

As a rule, this operation is not sufficient. The patients may have different body constitutions: fat / muscle ratio, pathologies, etc.

In this case we propose a transformation of the segmented reference model using several control planes and control points. At first, the user selects several control planes and tries to adapt the reference model in these planes. The model adaptation
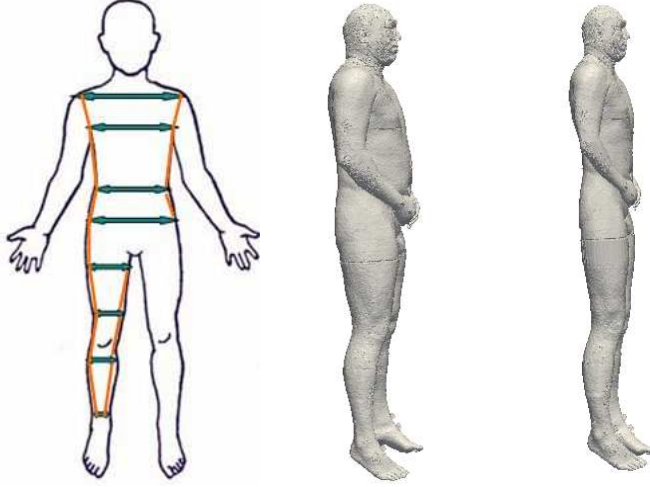
Figure 1. Anthropometrical rescaling of the human model.

in the plane is based on piecewise affine mapping defined by a set of control points. The user marks the same set of control points both on the reference image and on the patient image. Then he maps the reference image to the patient image shifting the control points from the original positions to the new ones. The control points may represent the anatomical or geometrical features of the human body. We assume that the anatomical structure of the segmented images of the reference model and the patient's model is the same. The size and the form of the individual's tissues may be varied using this adaptation.

The piecewise affine transformation is constructed on the basis of the Delaunay triangulation of the control points from the patient's image. The same triangulation with the identical topology is constructed using the corresponding control points in the reference image. Assuming the latter triangulation to be not tangled, we can construct the piecewise affine mapping of each triangle from one mesh to the corresponding triangle in the second mesh. An example of the transformed segmented image is presented in Fig. 2.

Once we have constructed the transformations on two parallel control planes (π_1 and π_2), we can define the transformation on any plane (π_α) between these planes using the linear combination of these two transformations as follows:

$$\varphi_\alpha^{-1}(\mathbf{x}) = \frac{1}{d}(\alpha\varphi_2^{-1}(\mathbf{x}) + (d - \alpha)\varphi_1^{-1}(\mathbf{x}))$$

where φ_1^{-1}, φ_2^{-1}, and φ_α^{-1} are the transformations in the planes π_1, π_2, and π_α; α is the distance between π_1 and π_α; d is the distance between π_1 and π_2.

An example of 3D transformation based on two control planes is presented in Fig. 3. This transformation was defined by two parallel control planes distanced 7 cm apart. Each plane has a set of control points. These points are placed in the way to decrease the outer fat tissues volume.
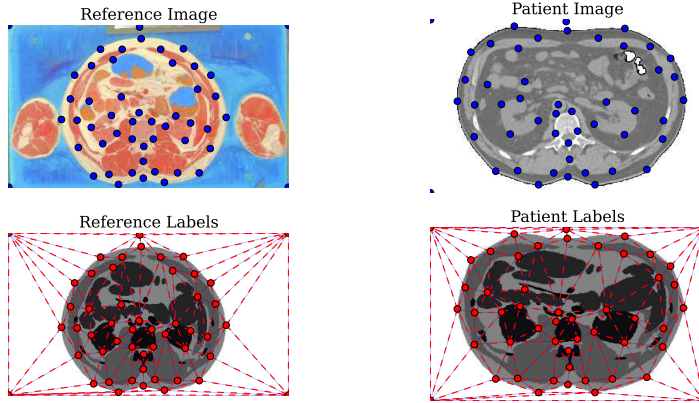
Figure 2. Control points mapping. Left: the reference segmented image with control points. Right: the mapped image with control points.
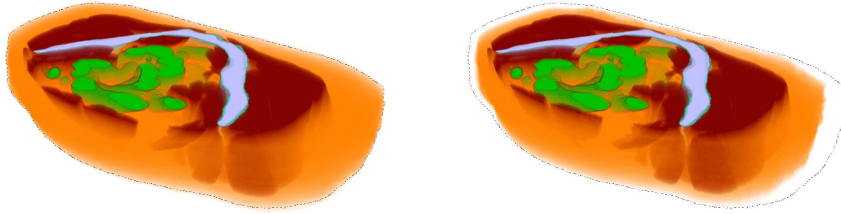
Figure 3. The pelvis region of the VHP Female 3D model between two parallel control planes. Control points mapping decreases the volume of outer fat tissues. Left: the reference segmented 3D model. Right: the mapped segmented 3D model with the dashed line representing the boundary of the reference model.

To make the piecewise affine transformation isomorphic, we assume that both Delaunay meshes are not tangled. If the user specifies the positions of the control points in such a way that the Delaunay mesh tangles, we propose to introduce additional auxiliary points. These points, in addition to the control points, are used to construct the Delaunay mesh. In contrast to the control points, the position of the auxiliary points is determined by the variational mesh modification method.

The mesh modification method is based on the assumption that a good mesh after modification has almost equilateral triangles. For any triangle we define its quality as [12]:

$$q = C \frac{S}{a^2 + b^2 + c^2}$$

where S is the signed triangle area; a, b, and c are the edge lengths; $C = 4\sqrt{3}$. Then for any triangle of a conformal mesh it holds $0 < q \leqslant 1$. If a triangle is degenerated, then $q = 0$. If a triangle of a conformal mesh is tangled, then $q < 0$.

For any auxiliary point with coordinates $\mathbf{x}$ we define the quality functional by

summing the host element (triangle) quality functionals

$$F(\mathbf{x}) = \sum_E F_E(\mathbf{x}), \qquad F_E(\mathbf{x}) = q_E^{-m}.$$

The parameter m controls the penalty for bad triangle quality. The function $F_E(\mathbf{x})$ grows as the element quality deteriorates and has a singularity at $q = 0$. In order to get rid of the singularity, we modify the triangle quality [6, 8]:

$$q^* = C\frac{h(S)}{a^2 + b^2 + c^2}, \qquad h(S) = \frac{1}{2}\left(S + \sqrt{S^2 + 4\delta^2}\right)$$

where δ is a positive parameter.

The functional

$$F_E^*(\mathbf{x}) = q_E^{*\,-m}$$

is positive and has no singularities even for tangled meshes. For a given decreasing sequence of δ, we shall move the auxiliary points to minimize the functional $F_E^*(\mathbf{x})$. Large values of δ are important for mesh untangling, and small values of δ are used for the triangle shape control.

The global minimization of the functional $F^*(\mathbf{x})$ is a difficult problem. Instead of solving this optimization problem, we apply pseudo-minimization: each auxiliary point is shifted along the anti-gradient of $F^*(\mathbf{x})$. The gradient of $F^*(\mathbf{x})$ is computed analytically.

If the E triangle is close to degenerate or tangled, the absolute value of $F_E^*(\mathbf{x})$ may be very large. If a point is shifted by a large distance, too many tangled triangles may appear and the iterative process will not converge. In order to guarantee the convergence, we damp the effect of large gradients by using the logarithmic function:

$$f(r) = \begin{cases} r, & r \leqslant r_0 \\ r_0(1 + \log(r/r_0)), & r > r_0. \end{cases}$$

The auxiliary point is shifted along the direction of the anti-gradient of $F^*(\mathbf{x})$ by the distance $f(|\nabla F^*(\mathbf{x})|)$.

The number of the auxiliary points needed to create a set of two untangled meshes may vary depending of the positions of the control points. In practice, if the control point movements are small enough, we do not need any auxiliary points. If the deformation is not very large, the number of the auxiliary points is not very large, either. The positions of the auxiliary points may be random, or they may be generated incrementally, every next point may be placed in the middle of the largest edge in the current Delaunay mesh.

3. Adaptation to the position of extremities

While the method with the control point shift is quite flexible, some model adaptation scenarios require additional work. An example is the adaptation of the model
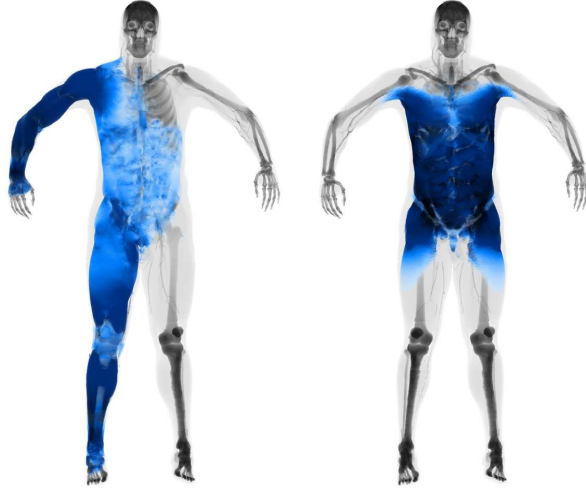
Figure 4. High sensitivity regions V_{97}^+, colored blue according to sensitivity value. Left: conventional tetrapolar measurement scheme. Right: eight-electrode parallel scheme for torso measurements.

Figure 5. The combined regions W_{97}^+ of contribution for ten-electrode scheme: arms along torso [3] (left), conventional position of arms (right).

with regard to the geometrical position of the body parts, e.g. the position of the arms, legs, or a standing/sitting position. In these cases one must perform particular segmented model transformations. Let us consider the modification of the arms position. Our proposal is to cut the arms along the virtual interface crossing the center of the shoulder joint. Each arm is rotated around the center of the shoulder joint. The overlapping parts are resolved based on the priority of the body parts or labeled tissues. The void sectors, occurring after the rotation, are filled with sweeping of the segmented image trace on the virtual cut surface.

In our previous work [3] we presented the results of sensitivity analysis for segmental bioimpedance measurements. This work was performed with the VHP segmented model of a man in his original position with his arms placed along the body. In practice these measurements are performed with the angle between the arm and the body nearly equal to $45°$. This angle may have some influence on the result of measurements.

In the present work we have adapted the initial model of the VHP man with respect to the conventional position of the arms. This adaptation was performed as described above. The constructed mesh has 479 198 vertices and 2 725 980 tetrahedra. We simulated bioimpedance measurements at the electrical current frequency 50 kHz using our FEM model. The electrical conductivity parameters for the labeled tissues were taken from [7].

The model has ten electrodes located in pairs on the forehead, both arms and both legs as described in [3]. The high sensitivity regions V_{95}^+ for the conventional tetrapolar scheme and the eight-electrode parallel scheme for torso measurements are presented in Fig. 4. The sensitivity field for the conventional tetrapolar scheme has a uniform sensitivity distribution near the shoulder as opposed to our previous results [3] obtained for the original model with the arms placed along the torso.

As we are interested in comparing our results to our previous model with parallel arms, we computed the sensitivity fields for all six segmental measurement schemes and combined their W_{97}^+ regions (see Fig. 5). The combined region represents the part of the body which may be accessed by at least one of these schemes. As opposed to our previous result, we do not observe blind zones in the lateral parts of the shoulders with the conventional position of the arms. These results indicate the importance of the empirically proposed arm position for segmental bioimpedance measurements.

Conclusion

In this work we have proposed the techniques for personalized model adaptation, including anthropometrical scaling, control points mapping and geometrical modification of the body extremities position. We have compared our previous results of segmental bioimpedance analysis using the VHP man model to the modified model with a corrected position of the arms. The numerical results demonstrate that the correct position of the arms is crucial for accessing the lateral parts of the shoulders. The modified model also shows a uniform sensitivity distribution near the shoulders for the conventional tetrapolar scheme. The proposed adaptation methods may be used for personalized BIA, as well as for BIA of a body with different positions of the extremities.

References

1. Advanced Numerical Instruments 3D. URL: http://sourceforge.net/projects/ani3d
2. L. Beckmann, D. van Riesen, and S. Leonhardt, Optimal electrode placement and frequency

range selection for the detection of lung water using bioimpedance spectroscopy. In: *Proc. 29th Annual Int. Conf. of the IEEE, Aug. 22–26* (2007) 2685–2688.

3. A. A. Danilov, V. K. Kramarenko, D. V. Nikolaev, S. G. Rudnev, V. Yu. Salamatova, A. V. Smirnov, and Yu. V. Vassilevski, Sensitivity field distributions for segmental bioelectrical impedance analysis based on real human anatomy. *J. Phys.: Conf. Ser.* (2013) **434**, 012001, doi: 10.1088/1742-6596/434/1/012001.

4. A. A. Danilov, D. V. Nikolaev, S. G. Rudnev, V. Yu. Salamatova, and Yu. V. Vassilevski, Modelling of bioimpedance measurements: unstructured mesh application to real human anatomy. *Russ. J. Numer. Anal. Math. Modelling* (2012) **27**, No 5, 431–440.

5. A. A. Danilov, V. Yu. Salamatova, and Yu. V. Vassilevski, Mesh generation and computational modelling techniques for bioimpedance measurements: an example using the VHP data. *J. Phys.: Conf. Ser.* (2012) **407**, 012004, doi: 10.1088/1742-6596/407/1/012004.

6. J. Escobar, E. Rodríguez, R. Montenegro, G. Montero, and J. González-Yuste, Simultaneous untangling and smoothing of tetrahedral meshes. *Comp. Meth. Appl. Mech. Engrg.* (2003) **192**, 2775–2787.

7. C. Gabriel, A. Peyman, and E. Grant, Electrical conductivity of tissues at frequencies below 1 MHz, *Phys. Med. Biol.* (2009) **54**, No. 16, 4863–4878.

8. V. Garanzha and I. Kaporin, Regularization of the barrier variational grid generation method. *Comp. Math. Math. Phys.* (1999) **39**, 1489–1503.

9. D. B. Geselowitz, An application of electrocardiographic lead theory to impedance plethysmography. *IEEE Trans. Biomed. Engrg.* (1971) **18**, No 1, 38–41.

10. S. Grimnes and O. G. Martinsen, *Bioimpedance and Bioelectricity Basics*. Elsevier, Amsterdam, 2008.

11. P. K. Kauppinen, J. A. Hyttinen, and J. A. Malmivuo, Sensitivity distributions of impedance cardiography using band and spot electrodes analyzed by a three-dimensional computer model. *Ann. Biomed. Engrg.* (1998) **26**, No 4, 694–702.

12. E. López, N. Nigro, and M. Storti, Simultaneous untangling and smoothing of moving and fixed grids. *Int. J. Numer. Meth. Engrg.* (2000) **10**, 1–6.

13. D. V. Nikolaev, A. V. Smirnov, I. G. Bobrinskaya and S. G. Rudnev, *Bioelectric Impedance Analysis of Human Body Composition*. Nauka, Moscow, 2009 (in Russian).

14. L. Rineau and M. Yvinec, A generic software design for Delaunay refinement meshing, *Comp. Geom. Theory Appl.* (2007) **38**, No. 1-2, 100–110.

15. Yu. V. Vassilevski, A. A. Danilov, D. V. Nikolaev, S. G. Rudnev, V. Yu. Salamatova, and A. V. Smirnov, Finite-element analysis of bioimpedance measurements. *Zh. Vych. Mat. Matem. Fiz.* (2012) **52**, No. 4, 733–745 (in Russian).

16. The Visible Human Project. URL: http://www.nlm.nih.gov/research/visible/

17. F. Yang and R. P. Patterson, A simulation study on the effect of thoracic conductivity inhomogeneities on sensitivity distributions *Ann. Biomed. Engrg.* (2008) **36**, No 5, 762–768.